Optics and Lasers in Engineering 195 (2025) 109303

Contents lists available at ScienceDirect

Optics and Lasers in Engineering

journal homepage: www.elsevier.com/locate/optlaseng

Chessboard-based achromatic binary Zone Plate

Sara Fernandez-Nuñez [a,*], Jose Antonio Gomez-Pedrero [a], Francisco Jose Torcal-Milla [b,c], Luis Miguel Sanchez-Brea [c]

[a] Applied Optics Complutense Group, Optics Department, Facultad de Óptica y Optometría, Universidad Complutense de Madrid, C/ Arcos de Jalón 118 28037, Madrid Spain

[b] Grupo de Tecnologías Ópticas Láser, Instituto de Investigación en Ingeniería de Aragón, Escuela de Ingeniería y Arquitectura, Universidad de Zaragoza, C/ Pedro Cerbuna 12 50009, Zaragoza Spain

[c] Applied Optics Complutense Group, Optics Department, Facultad de Ciencias Físicas, Universidad Complutense de Madrid, Plaza de las Ciencias 1 28040, Madrid Spain

ARTICLE INFO

Keywords:
Diffractive optical elements
Chromatic aberration
Binary phase plate

ABSTRACT

We numerically and experimentally demonstrate the performance of a new kind of diffractive binary zone plate for chromatic aberration compensation: the chessboard-based zone plate. The proposed achromatic zone plate consists of two spatially multiplexed zone plates following the geometry given by a chessboard and improved with morphological filters and combination under the Nyquist frequency, to mitigate aliasing effects. The obtained results are compared with those given by a random pixel-based multiplexed zone plate, reported in the literature, showing similar optical behaviour. However, the chessboard-based zone plate presents a smoother appearance without the high-frequency irregularities of the random-based designs that could be more resistant to manufacturing errors. The proposed achromatic zone plate could result of interest in fields such as solar concentration, lithography, imaging systems, visual optics, and so on.

1. Introduction

The chromatic dispersion properties of common optical materials, such a glass or plastic, not exhibiting anomalous dispersion, causes refractive lenses made of them to focus blue light before red light. In contrast, diffractive lenses, such as Fresnel Zone Plates (FZP), focus red light nearer than blue. In both cases, it results in chromatic aberration. Chromatic aberration degrades the optical quality of any optical system, even when all other aberrations are corrected [1]. As a result, a lot of effort has been dedicated to correct chromatic aberration, particularly in imaging applications, although it could also be problematic for non-imaging optical systems [2]. In purely refractive systems, chromatic aberration is compensated by combining lenses of different powers made of materials with varying Abbe numbers and, therefore, inverse chromatic dispersions [1]. These combinations result in achromatic, apochromatic, or superachromatic systems [3]. An optical system is defined as achromatic when the focal points for two different wavelengths—typically at both ends of the visible spectrum—coincide. In an apochromatic system, the focal point is the same for three distinct wavelengths, whereas a superachromatic system achieves a common focal point for more than three wavelengths. Chromatic aberration can also be corrected by combining refractive and diffractive optical elements. In this case, the goal is taking advantage of the opposite chromatic dispersion properties of refractive versus diffractive optical elements. This property is used in certain designs, such as high-performance photo lenses [4–6], super-achromatic cylindrical lenses [7], harmonic lenses [8], or even varifocal telescopic systems based on Alvarez lenses [4].

A third strategy for correcting chromatic aberration relies on multiplexing. Optical multiplexing comprises several techniques for combining optical signals in a wide range of applications. For example, optical multiplexing is used in the field of integrated optics to expand the capabilities of silicon-based hybrid demultiplexers for wavelength- and mode-division multiplexing [9], a concept that has been expanded to include polarization division by Yu et al [10]. Optical multiplexing also has applications in optical communications, where digital power domain multiplexing of orthogonal frequency division multiplexed, signals is used to achieve high data rates [11]. For purely diffractive optical systems corrected for chromatic aberrations, two strategies, temporal and spatial multiplexing, have been reported in the literature. Temporal multiplexing employs programmable devices, such as Spatial Light Modulators (SLMs), to dynamically change the focal properties of

* Corresponding author.
E-mail address: sarafn@ucm.es (S. Fernandez-Nuñez).

https://doi.org/10.1016/j.optlaseng.2025.109303
Received 5 June 2025; Received in revised form 13 August 2025; Accepted 22 August 2025
Available online 28 August 2025

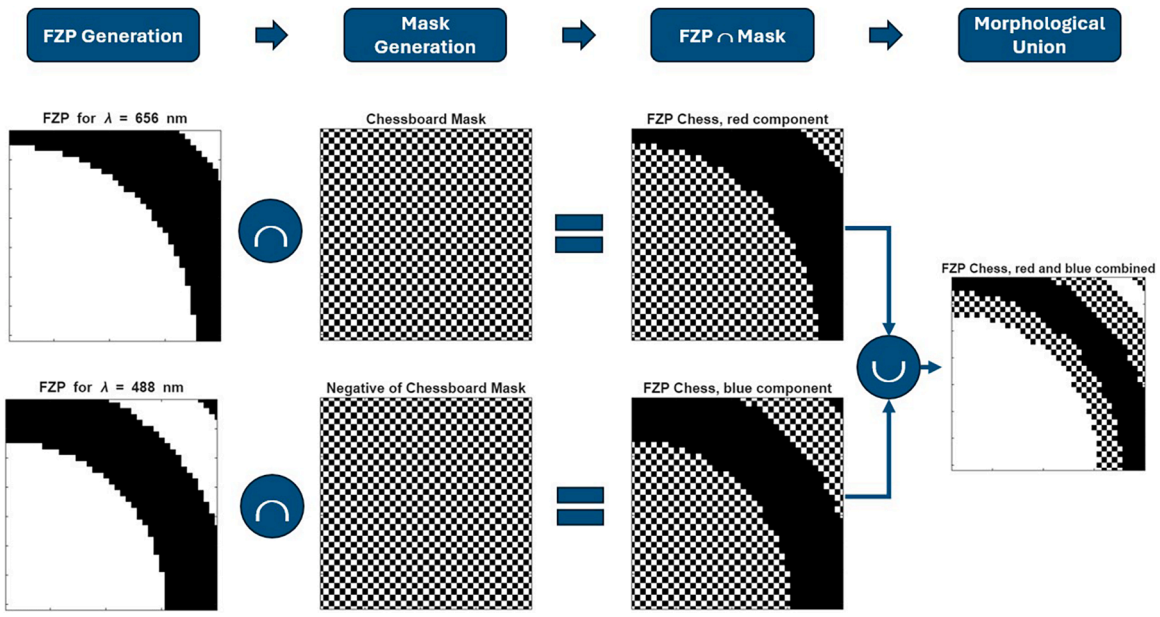

Fig. 1. Illustration explaining the chessboard multiplexing. The binary FZP mask computed for the C and F wavelengths are combined with the positive and negative chessboard mask through an intersection ("and") logical operation. The resulting red and blue components are combined by means of a union ("or") logical operation. Notice the binarization noise introduced by this procedure in the boundaries of the Fresnel zones.

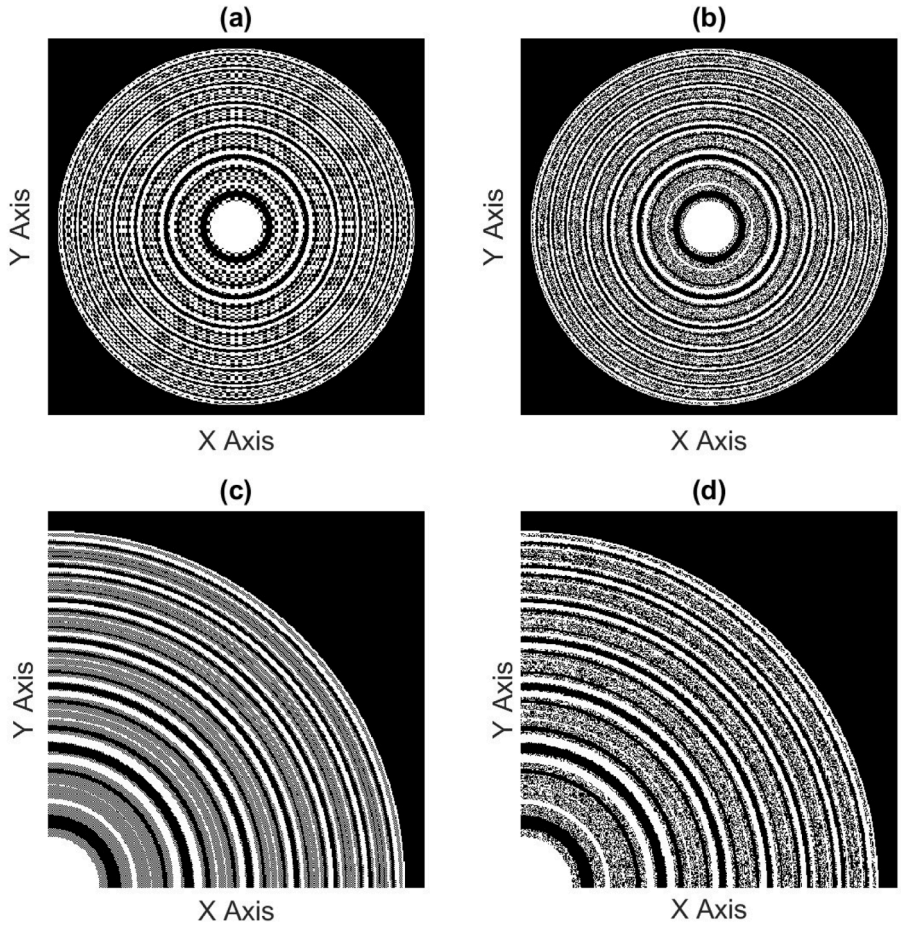

Fig. 2. Phase map of a 6 mm diameter achromatic Fresnel zone plate with a focal length of 380 mm, designed for the red (Fraunhofer C line) and blue (Fraunhofer F line) wavelengths. The zone plate is constructed using two combination strategies: (a) a chessboard-based pattern and (b) a random pixel-based pattern, for spatially combining the FZPs designed for the red and blue wavelengths. Panels (c) and (d) show magnified views of the phase maps corresponding to the chessboard-based and random pixel-based patterns, respectively. The phase map is normalized between 0 and 1, where 1 corresponds to a phase jump of π radians. The grey areas visible in panel (c) are due to a dithering effect.

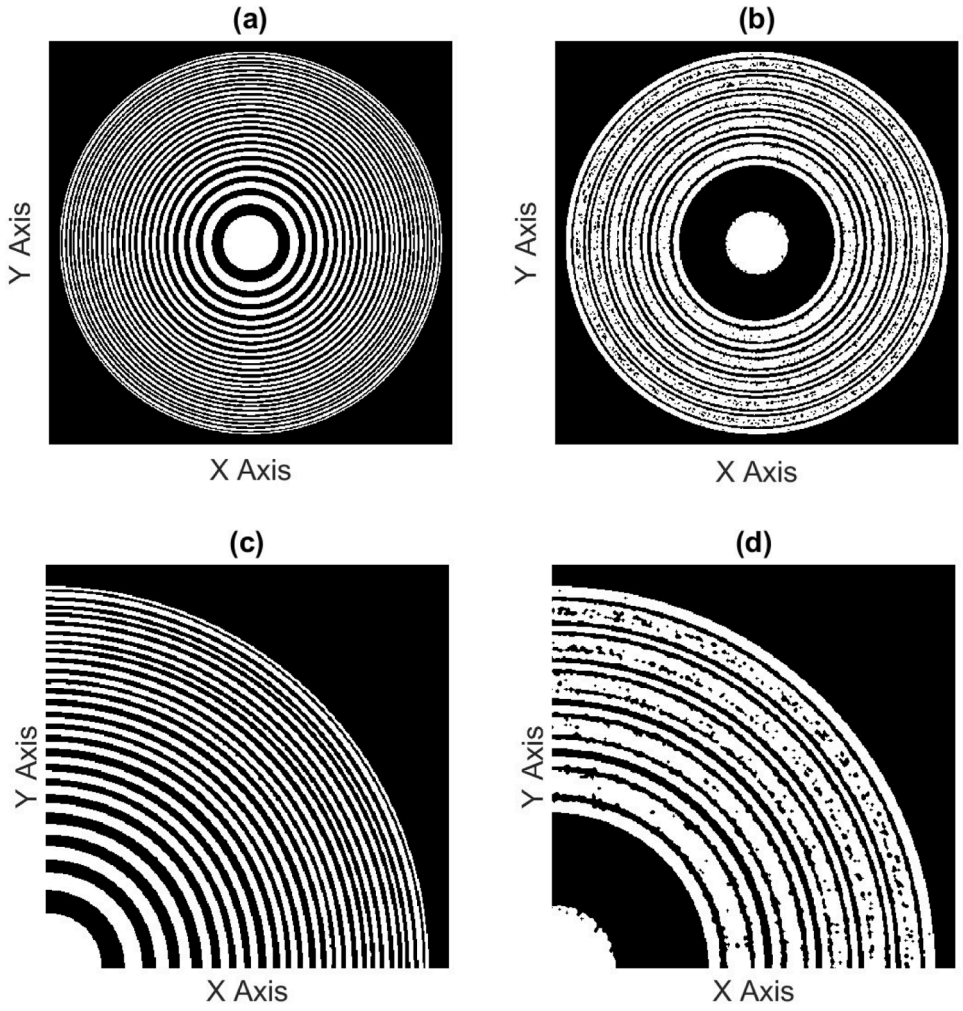

Fig. 3. Phase maps obtained after application of sub-Nyquist frequency multiplexing and morphological filtering to the phase maps shown in Fig. 2. a) Achromatic chessboard-based zone plate, and b) Achromatic random pixel-based zone plate with sub-Nyquist multiplexing and morphological processing, c) and d) magnified detail of these zone plates showing that, for the random Achromatic zone plate, d), some binarization noise remains. Notice that the phase map is normalized between 0 and 1, where 1 corresponds to a phase jump of π radians.

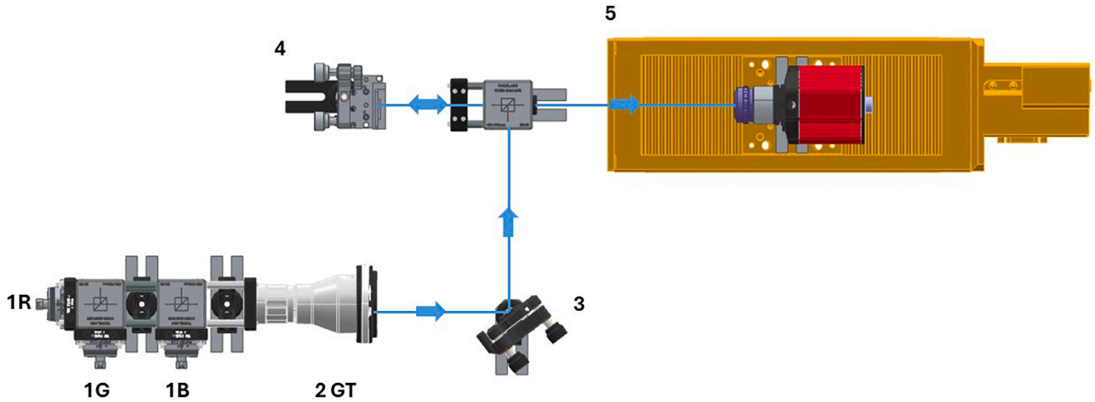

Fig. 4. Schematics of the experimental set-up with the following parts: 1) illuminating system formed by three fibre ports for the red (1R), green (1 G) and blue (1B) pigtailed-laser diodes, combined by beam splitters in a common path (blue line) and expanded with a 2) 5x Galilean Telescope (GT), 3) main mirror, 4) PLUTO SLM and 5) CCD camera mounted on the linear motorized stage.

the lens for different wavelengths, effectively averaging focal adjustments over an exposure period [12,13]. Although effective, this approach requires precise synchronization between the SLM's refresh rate and the camera exposure, limiting its practicality for rapid or continuous measurements or visualization.

Spatial multiplexing is a technique used to design diffractive optical elements by combining simpler designs, such as a Fresnel zone plate. This combination can be used in several ways. For example, Kazanskiy et

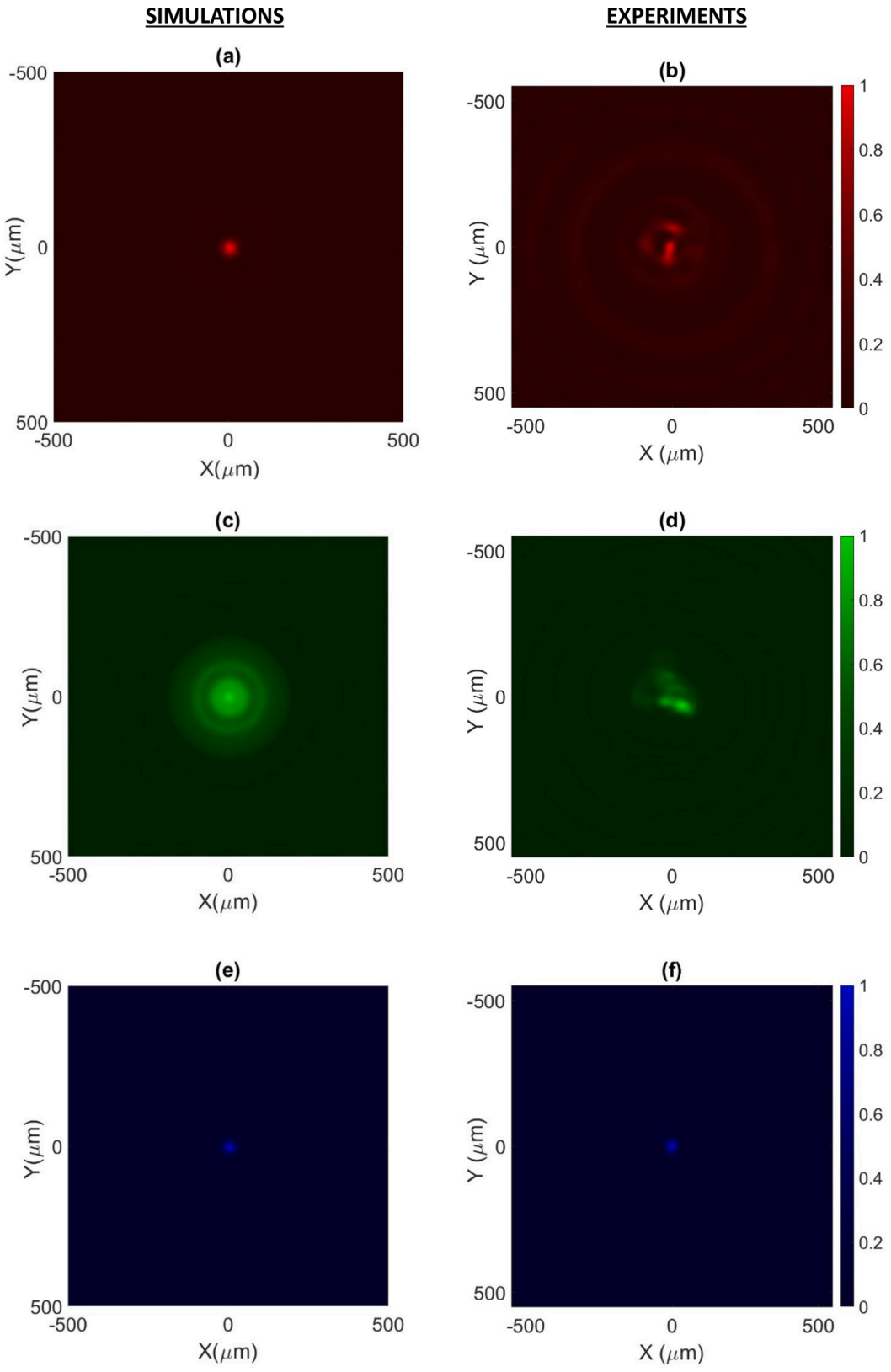

Fig. 5. Simulated beam profile (left column) at the focal distance of 380 mm of the chessboard-like zone plate for the a) red, c) green, and e) blue beams, and experimental beam profiles for the b) red, d) green, and f) blue wavelengths.

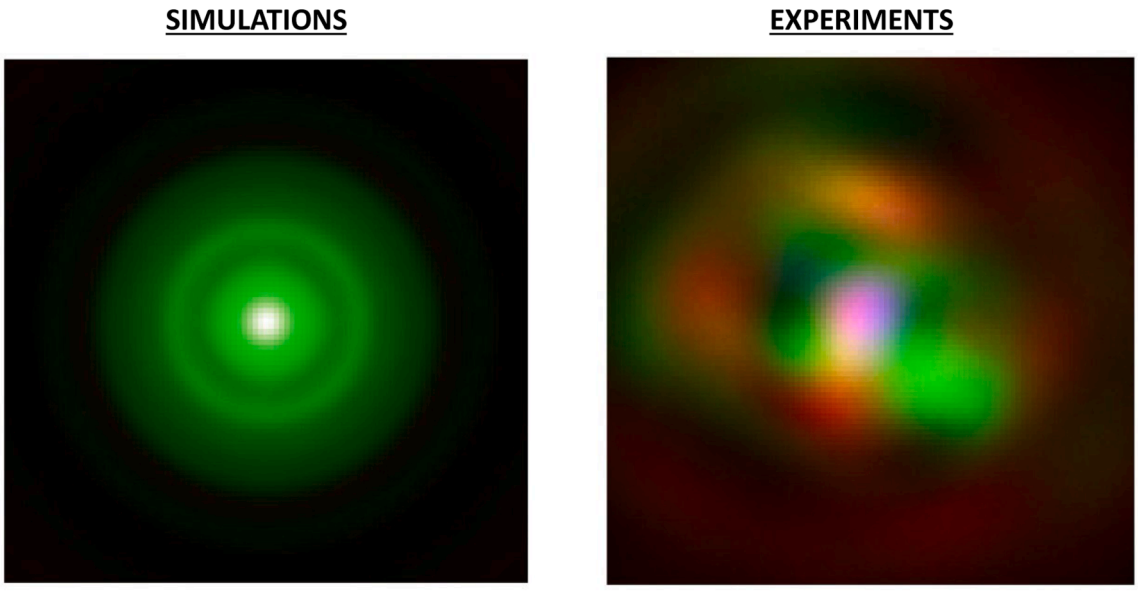

Fig. 6. Composed intensity map obtained by combining the intensities given in Figs. 5a), c) and e) for the simulated RGB bean profile at the left, and Figs. 5b), d) and f) for the experimental one at the right.

al [14] form a complex beam-divider by a linear combination of different gratings, each optimized for a given spatial frequency. A similar approach is followed by [15,16] for designing optical phased arrays for beam steering. Rosen et al [17] presents a new methodology called Transport of Amplitude into Phase using the Gerchberg-Saxton Algorithm (TAP-GSA) for designing multifunctional pure phase DOEs.

Another approach for spatial multiplexing dividing the lens into multiple regions, with each region corresponding to a simple design, such as a Fresnel zone plate, with different properties among them. This approach has been followed [18,19] for designing achromatic zone plates, in this case, each region is optimized to focus a specific wavelength and therefore achieve achromaticity. This method is entirely passive, making it both robust and cost-effective. For example, Marquez *et al* [20] proposed a couple of multiplexing schemes for obtaining apochromatic diffractive lenses by combining three standard lenses —each designed for a different wavelength—into a single-phase distribution. One strategy divides the monochromatic lenses into rings and sectors while the second strategy combines the monochromatic lenses pixelwise following a random pattern. In a later study, Marquez et al [21] demonstrated that these lenses can be manufactured as FZPs. However, the resulting FZPs appear rather noisy, thus introducing secondary foci with the consequent image degradation, even if the apochromatic condition is met.

Other strategies for multiplexing include recent metasurfaces developments. Eisenbach et al., for instance, achieved broadband achromatic focusing through advanced metasurface integration [22]. A similar strategy is employed by other authors [7], while Luo *et al* [23] combine diffractive optical elements with polarization optics for compensating chromatic aberration in liquid-crystal optics. Such innovations highlight the progress and interest in creating highly functional achromatic lenses using spatial multiplexing.

In this work, we propose a novel approach to design achromatic binary FZPs using the following spatial multiplexing strategy. First, we propose a chessboard-based pattern for the achromatic phase distribution. It takes also advantage of the squared shape of the pixels when opto-electronic devices are used. Second, to minimize high diffraction orders, we combine the monochromatic lenses beyond the Nyquist frequency. Finally, we apply morphological filtering to remove binarization noise, improving manufacturability. Numerical simulations and experiments demonstrate the effectiveness of our design.

2. Theoretical analysis and design principles

Fresnel Zone Plates (FZPs) are diffractive optical elements that act similarly to a conventional converging refractive lens [1,6]. They have advantages such as lightness, compactness, customizable optical properties, and cost-effective manufacturing, that make diffractive lenses useful for a wide range of applications. Note that the FZP can be defined as amplitude-based or phase-based zone plate. In any case, a conventional Fresnel Zone Plate is composed by a set of concentric rings of radii given approximately by

$$r_n \cong \sqrt{n\,\lambda f}_{n=1,2,\ldots}, \tag{1}$$

where n is the order of the ring, λ is the wavelength of the impinging light, and f is the design focal distance of the Fresnel Zone Plate. From Eq. (1), we observe that the Zone Plate is designed for a single wavelength. Therefore, light is focused at the distance f only for this design wavelength. Other wavelengths will focalize at other distances [6], resulting in chromatic aberration.

In this work, we focus on spatially multiplexed achromatic Fresnel Zone Plates, specifically binary phase zone plates. Thus, we define the FZP as a binary mask that models a π radian phase shift between adjacent zones. Specifically, the binary mask corresponds to the actual phase function divided by π, resulting in alternating values of 0 and 1. Notice, that, as a pure phase element, the FZP transmits light uniformly across its entire aperture.

The general principle of spatial multiplexing relies on generating a set of FZPs, all of them designed for a given focal length but different wavelength. Therefore we start with a set of binary plates

$$\left\{FZP\left(x,y;f,\lambda_j\right)\right\}_{j=1,2,\cdots N}, \tag{2}$$

where f is the focal length, common for all plates of the set, λ_j the design wavelength for the j-th phase plate, and N is the number of phase plates. Each FZP is defined in a discrete grid of dimensions $\left\{N_x \times N_y\right\}_{j=1,2,\ldots N}$ being each pixel a square of Δx width. In order to combine these FZPs into a single binary phase plate, we define a set of mutually exclusive binary masks $\left\{B_j\right\}_{j=1,2,\ldots N}$ such that $B_i \cap B_j = \varnothing\ \forall i \neq j$ and $\cup_{j=1}^{N} B_j = E$, where E is a binary matrix with all elements equal to one. Under these conditions, the combined, or multiplexed FZP is defined as

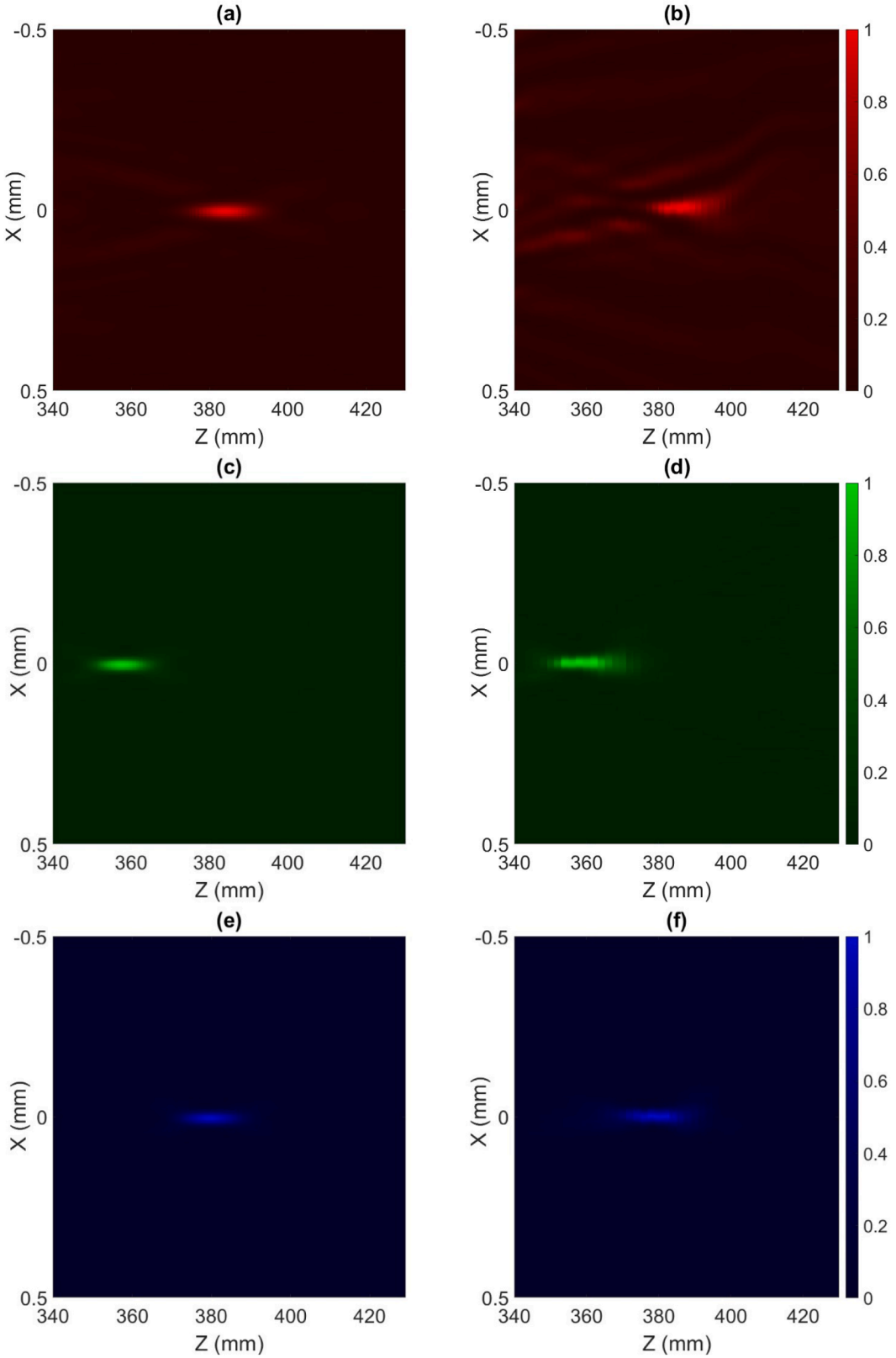

Fig. 7. Beam tomographies, for the chessboard-like achromatic lens into the X-Z plane for both simulation, panels a), red, c) green, and e) blue, and experiment, panels b) red, d) green and f) blue.

$$FZP_{mult}(x,y|f) = U_{j=1}^{N}\left[B_j \cap FZP(x,y;f,\lambda_j)\right]. \quad (3)$$

In this paper, we propose achromatic FZPs by combining two wavelengths corresponding to the Fraunhofer lines C and F. Therefore, in this case, the set of exclusive binary masks is $\{B,\overline{B}\}$ where B is the mask for the Fraunhofer line C, and $\overline{B}$ its complementary. Mask B can be defined in several ways. Marquez et al [20] use a pixel-wise random pattern. In this work, we instead use a chessboard-based pattern. We will

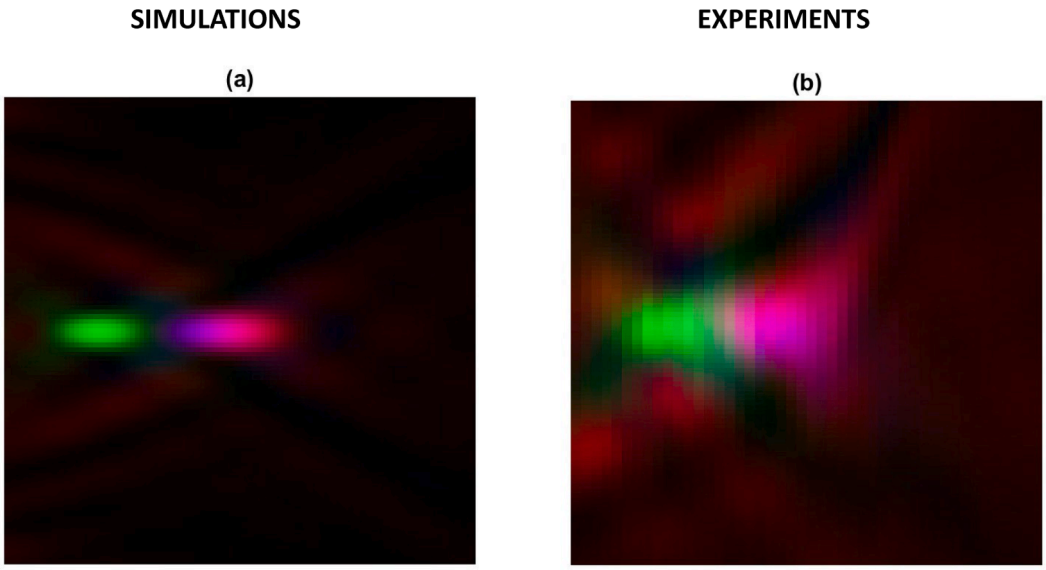

Fig. 8. Composed intensity map obtained by composing the intensities given in Fig. 7 into an RGB tomographic profile of the beam generated by the chessboard-like lens for both simulation (left) and experiment (right).

discuss the implications of these different designs later in the paper.

Although the procedure described above allows the design of chromatic corrected zone plates, the resulting patterns often exhibit a noisy appearance [20,21]. Either random and structured patterns, such as chessboard-based designs, lead to jagged edges at the boundaries of the circular zones (see Fig. 2). These imperfections cause diffractive scattering, reducing contrast and generating secondary foci near the primary focus [24,25]. In addition, the fine details required for these patterns pose manufacturing challenges, particularly without the use of expensive photolithographic techniques.

To overcome this issue, we have devised two strategies. First, we perform the spatial multiplexing below the Nyquist frequency. To achieve this, both the set of FZPs set $\{FZP(x,y;f,\lambda_j)\}_{j=1,2}$, and the corresponding set of complementary masks $\{B,\overline{B}\}$ are defined on a grid of size $[2N_x \times 2N_y]$, with a pixel width equal to $\Delta x/2$ (assuming square pixels). After combining the FZPs with the set of multiple exclusive masks, as described in Eq. (3), we apply a moving average convolution filter over a 2×2 neighbourhood to mitigate aliasing artifacts [26]. Finally, the filtered result is decimated to the original sampling size of $[N_x \times N_y]$.

In Fig. 1 we show an illustration of the chessboard multiplexing showing the intersection of the two zone plates with their corresponding checkerboard mask (the mask for the blue channel is the negative of that for the red one) to get the red and blue components of the achromatic FZP and then, the combination of these components in a single binary mask.

Afterwards, we perform a morphological processing to the resulting binary matrix that defines the FZP. The goal is to reduce the jagged edges and the "binarization noise" of the FZP to improve the manufacturability of this kind of zone plates. In general, a FZP is composed of a series of concentric rings of decreasing width. As shown in Figs. 1 and 2, the spatial multiplexing respects this ring structure but adds binarization noise.

To reduce binarization noise and other irregularities, the morphological processing consists of three main stages:

1. **Preliminary morphological operations**: An opening followed by a closing operation is applied using a disk-shaped structuring element with a radius of 1 pixel. These operations help smooth the binary mask and remove small artifacts within the rings.
2. **Area-based filtering**: Regions with an area below a predefined threshold are identified and removed, eliminating small, isolated components unlikely to belong to the intended zone plate structure.
3. **Circularity-based filtering**: Regions that significantly deviate from the expected circular shape of the Fresnel zones are detected and removed based on a circularity metric.

Circularity metric is an indicator of how the shape of a connected region resembles a circle, or, in our case, also an annulus. It is computed as

$$c = \frac{4\pi A_{convex}}{P^2}, \tag{4}$$

where A_{convex} is the convex area, defined as the area of the smallest convex shape enclosing the region's perimeter, and P its perimeter. We have used the convex area instead of simply the area of the region as, in our case, Fresnel zones are typically rings, which would otherwise result in misleadingly low circularity values. As the maximum value of the circularity metric is $c = 1$, corresponding to a perfect circular (or annular) object with large area, we set a threshold and remove those regions whose circularity falls below this threshold.

This sequence of operations preserves the key structural features of the FZP while effectively minimizing noise and spurious elements introduced during binarization.

In Fig. 3 we show the result of applying the procedure described above to the achromatic FZP designs shown in Fig. 2. In the case of the chessboard-based pattern, Figs. 3a) and 3c) show a clean phase map formed by concentric rings with an appearance quite like a standard FZP. Despite this resemblance, the ring width and distribution is, effectively, a combination of the distribution and sizes of the rings of two conventional FZPs designed for the red and blue wavelengths, although it is difficult to appreciate this in Figs. 3a) and 3c). Clearly, the phase map of the chessboard-based pattern presents a smother appearance and the effects of binarization noise are not present either.

However, the lens designed from random pixel-based patterns presents additional problems. Firstly, the morphological filter does not work as well as it did with the chessboard-based lens, as binarization noise is still present as it can be appreciated in Figs. 3b) and d). Moreover, as the random pixel-based pattern design is based on a stochastic process, the final lens obtained varies with each running of the generation algorithm. This is an important issue, that limits the usefulness of

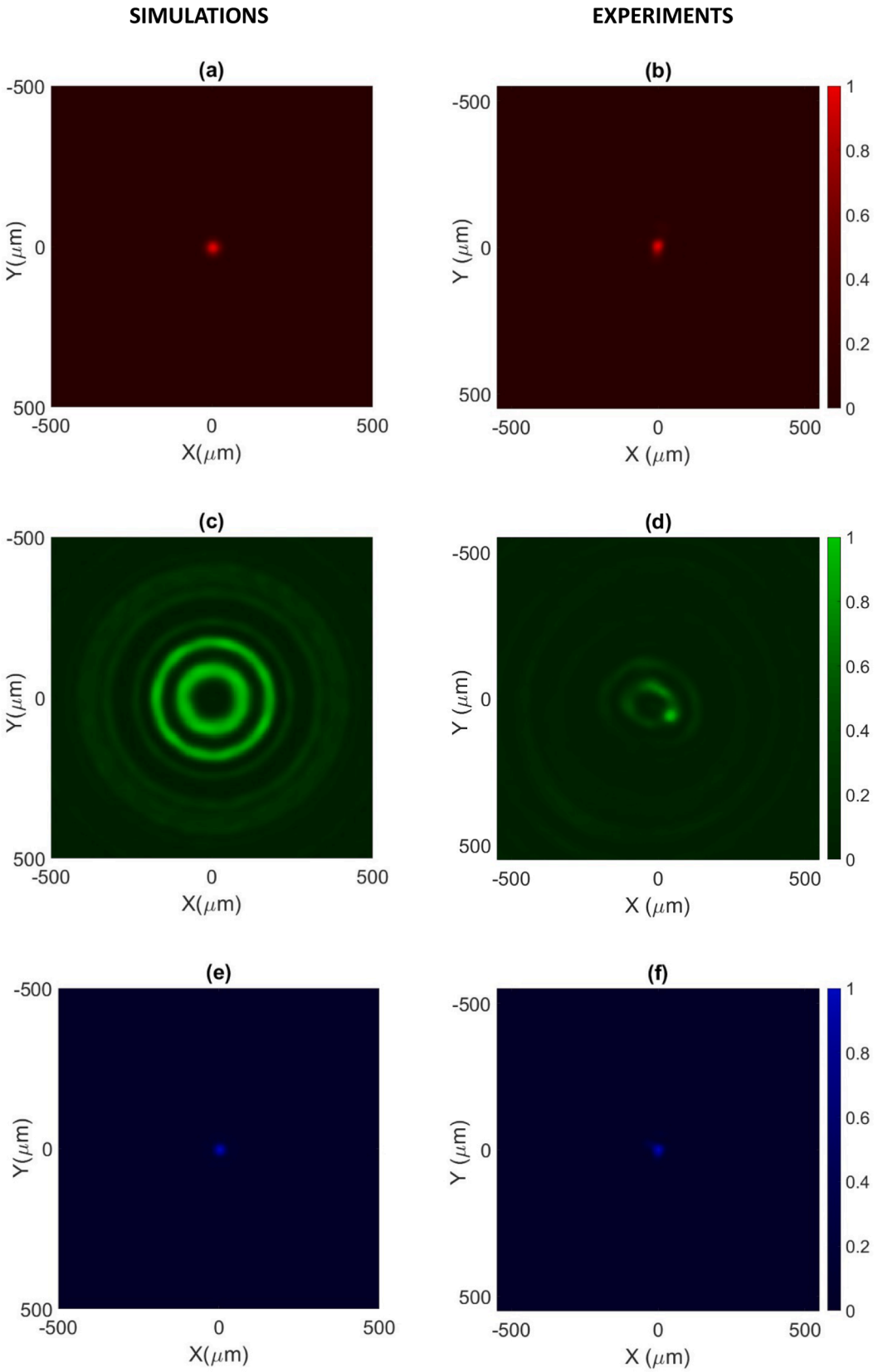

Fig. 9. Simulated beam profile (left column) at the focal distance of 380 mm for the a) red, b) green, and c) blue beams, and experimental ones: b) red, d) green, and f) blue beams, for the realization of the random pixel-base achromatic Fresnel Zone Plate shown in Fig. 3b).

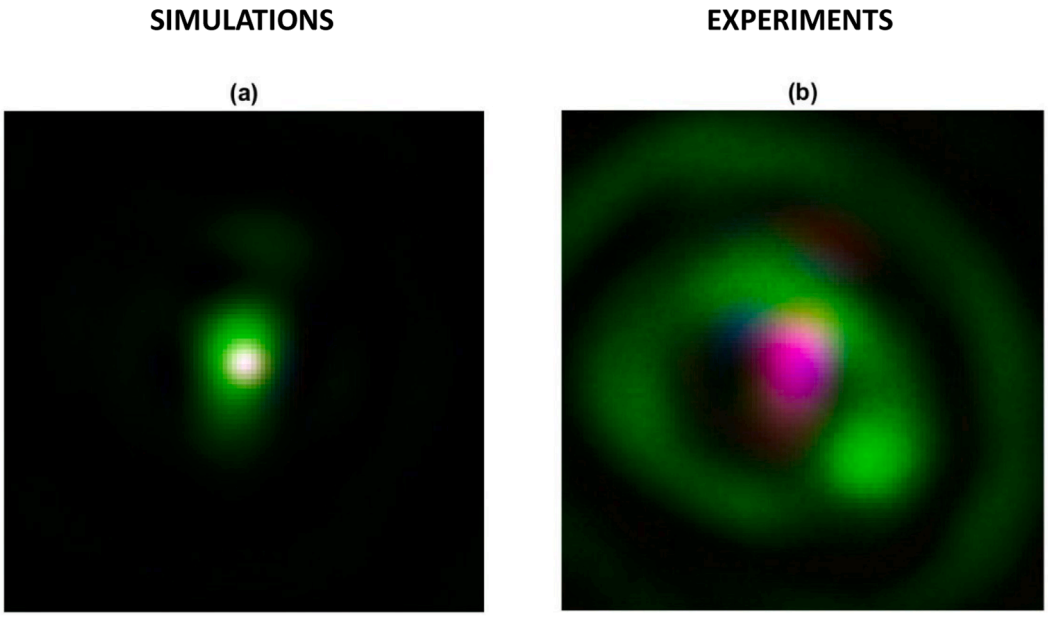

Fig. 10. Composed intensity map obtained by composing the intensities given in Fig. 9 into a RGB image for both simulated (left) and experimental (right).

these random pixel-based designs. At this point, it is important to notice that we will analyse the properties of the random pixel-based lens realization shown in Fig. 3b). However, the reader should be advised that this is not a unique realization of this lens, so some variations on the optical properties can be expected if other realizations are selected. In what follows, we will study the optical properties of both the chessboard-based and random pixel-based designs with both computer simulations and experiments.

3. Methods

We have tested the achromatic designs proposed in the previous section through both simulations and experiments. In the simulation, we sampled the phase distribution of each lens on a grid of 1920 × 1080 square pixels, each with a width of 8 μm. Additionally, the phase of the lens was quantized into 128 grey levels, corresponding the 128 grey level to a phase jump of π. This approach allowed us to replicate the properties of the spatial light modulator (SLM), PLUTO-2-NIR-11 [27], used in the experiment. The simulation was conducted in MatLab, using the Bluestein propagation algorithm as implemented by Hu et al [28, 29]. The advantage of the Bluestein algorithm is that permits different sampling between object and image planes. All simulations were performed using MATLAB 2023b on an i7-Core computer with 32 GB of RAM. The computing time for the simulation of a tomographic profile composed by 101 images was around 115 s.

Fig. 4 illustrates the experimental setup used to measure the chromatic properties of the proposed diffractive zone plates. The setup includes three pigtailed laser diodes with peak wavelengths of 488 nm, 518 nm, and 658 nm, respectively. These wavelengths were chosen to closely match (when possible) Fraunhofer's spectral lines C (656 nm - red), d (587 nm - green), and F (486 nm - blue), which are commonly used to characterize the chromatic properties of image-forming systems. The usage of a wavelength located in the centre of the spectrum is useful for estimating the residual chromatic defocus or "secondary colour" of an achromatic system. Secondary colour is usually defined as a focal shift between the common foci corresponding to the F and C spectral lines and the focus corresponding to either the d-line (589 nm) or e-line (546 nm), and it quantifies the broadband chromatic response of an achromatic optical system. Each laser diode is collimated by a Thorlabs fibre optics port, model PAF2P-11B for the red beam, and model PAF2P-11A for both the green and blue beams. The collimated beams are combined into a common path using a system of beam splitters (see part 1 of Fig. 4). Afterwards, they are expanded using a 5x Galilean telescope (labelled as GT in Fig. 4) and, after passing through a linear polarizer, are directed by a plane mirror towards the SLM (Spatial Light Modulator) PLUTO-2-NIR-11 (see part 4 of Fig. 4). The beam reflected from the SLM is captured by a CS135M Thorlabs CMOS camera which has a sensor resolution of 1280 × 1024 square pixels, each one with a width of 4.8 μm, mounted on a linear motorized stage (model 8MT175–200-Men1), manufactured by Standa (part 5 of Fig. 4). The experimental system is designed to measure the tomography of a laser beam near the focal point of the designed zone plates implemented in the SLM. The measurement is performed sequentially, starting with the tomography of the red light, followed by the green and blue ones.

To obtain a single tomography, a discrete set of transverse sections of the beam is captured at different positions of the CMOS sensor along the optical axis. In the next section, we describe and discuss the obtained results, simulated and experimental.

4. Results

For both zone plate designs—the previously published random pixel-based and the proposed chessboard-based FZPs—we begin by comparing the experimental and simulated intensity distributions for three wavelengths (488 nm, 518 nm, and 658 nm) in a plane located 380 mm from the zone plate. This distance corresponds to the design focal length for both the red and blue wavelengths. Next, we present the beam tomography (both experimental and simulated) for each wavelength individually. Finally, we compare the on-axis intensity profiles (i.e., the intensity at the beam centroid along the optical axis) for the two achromatic designs. For completeness, we also include measurements of a standard Fresnel zone plate with the same focal length, designed for a single wavelength of 518 nm.

As we have mentioned in the previous section, the chessboard-based zone plate is of the type shown in Fig. 3a). Fig. 5 presents the simulated intensity distribution -panels a) red, c) green, and e) blue wavelength- and the corresponding experimental intensity distributions -panels b), d), and f)- at the common red/blue focal point, located 380 mm from the SLM. In both cases, it can be observed that the red and blue beams are well-focused, demonstrating the achromatic design of the zone plate. Additionally, we have simulated and measured the propagation of the green beam, Figs. 5c) and 5d), respectively, which is obviously

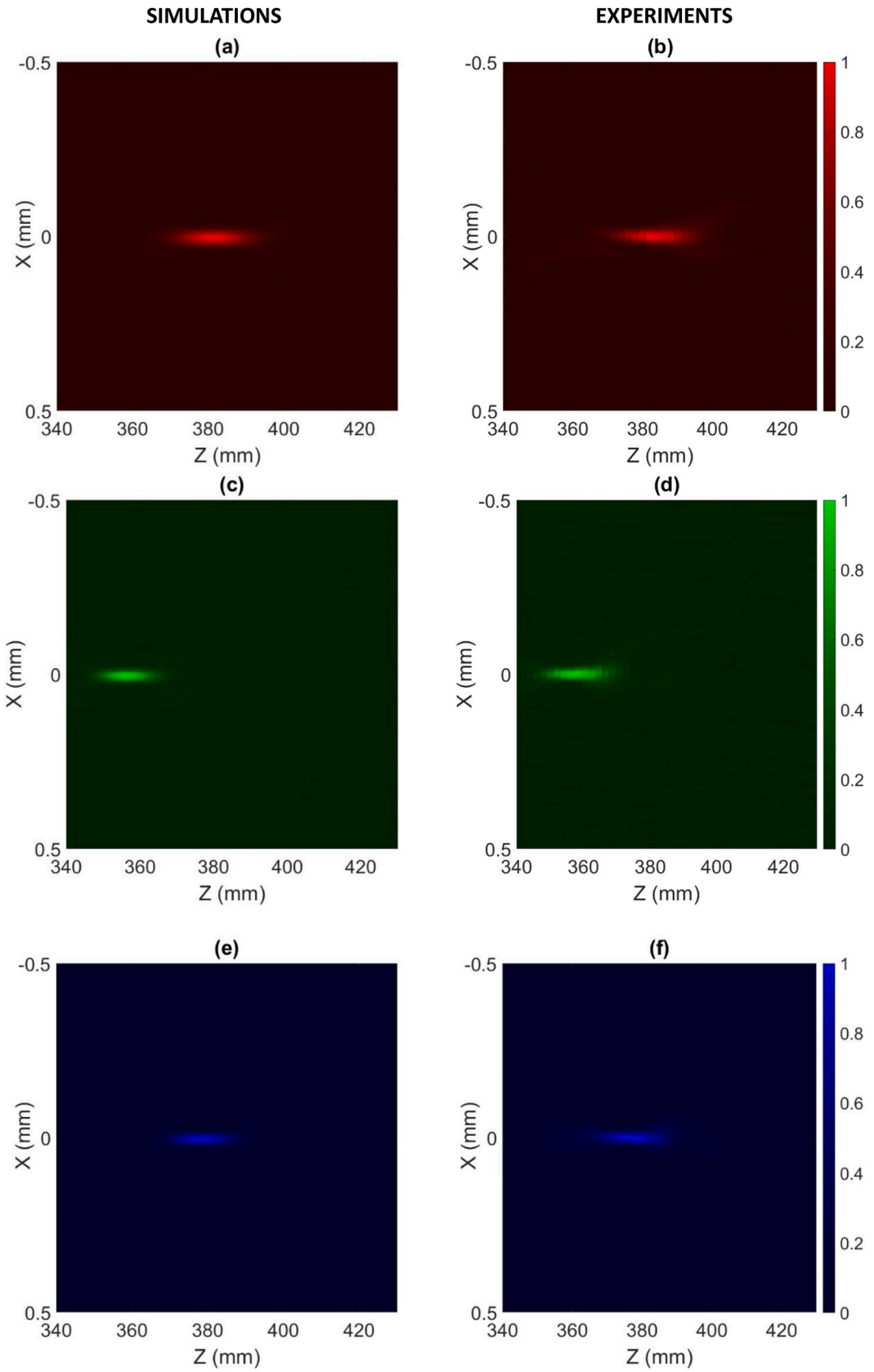

Fig. 11. Simulated beam propagation (left column) along the optical axis for the a) red, c) green, and e) blue beams, and experimental ones for the b) red, d) green, and f) blue beams, corresponding to the random pixel-based Achromatic Fresnel Zone Plate.

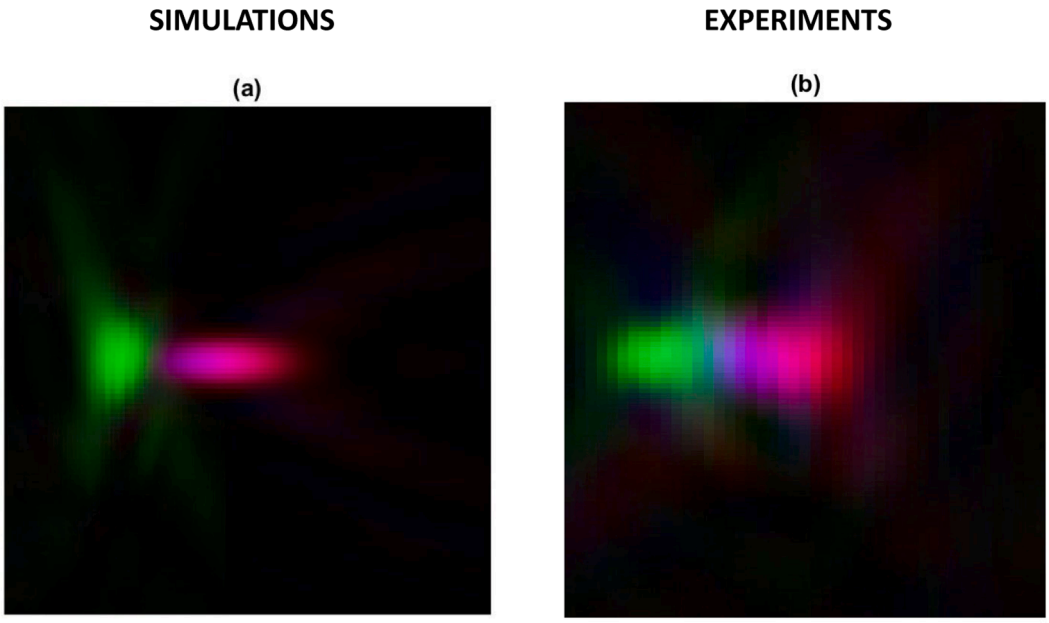

Fig. 12. Composed intensity map obtained by adding the intensities given in Fig. 11.

defocused at that distance. However, although the general shape of the experimental and simulated beam intensity distributions is similar, the experimental results show some discrepancies. For example, when comparing panels, a) and b) in Fig. 5, which correspond to the red beam, differences in the intensity distribution can be observed. In the simulated case, Fig. 5a), the beam displays perfect discrete rotational symmetry, whereas in the experimental case, Fig. 5b), the intensity distribution is elongated along the x-axis. This discrepancy could be attributed to aberrations introduced by the optical system, especially the spatial light modulator, particularly astigmatism. For completeness, a composed intensity field is shown in Fig. 6, where the intensities for the red, green and blue beams (Fig. 5) have been combined in a RGB composite image. As it can be observed, the experimental one exhibits a central zone almost white showing its achromaticity, that resembles the simulated behaviour acceptably. The plots of Fig. 6 are magnified, compared to that of Fig. 5, therefore only the region around the optical axis is shown, which accentuates the effect of aberrations and, also displacement between beams in the experimental setup. Therefore, these images are only useful to prove the achromaticity of our design.

Fig. 7 shows the X-Z plane beam tomographies for both simulations and experiments. In both cases, the tomographies of the red beam -panels a) and b) in Fig. 7- and blue beam -panels e) and f) in Fig. 7- reveal a common focal point located around 380 mm from the zone plate, again proving the achromatic design of the chessboard-based achromatic zone plate. Additionally, we observe in Figs. 7c) and 7d) that the green beam focuses closer to the zone plate, as expected from the design. For completeness, a composed intensity field is shown in Fig. 8, where the intensities for the red, green and blue beams (Fig. 7) have been combined to form an RGB image.

Next, we analyse the results obtained for a random pixel-based zone plate. Particularly, we have tested the realization shown in Fig. 3b). These zone plates are designed with the same achromatic concept as the chessboard-based achromatic zone plates and therefore they exhibit a common focal distance for the red and blue beams, located around 380 mm from the zone plate, as shown in Fig. 9a), 9b), 9e) and 9f). Additionally, the focal point for the green beam appears defocused, Fig. 9c) and 9d). The primary difference between the chessboard-based and random pixel-based zone plate designs is the uniqueness of the chessboard-based design, whereas the random pixel-based zone plates are not unique, as each computation of a random pixel-based zone plate generates a slightly different design. However, as the randomness scale is related to the pixel size, we expect that the behaviour of the different realizations of the random pixel-based zone plate does not differ in its basic optical properties. For completeness, a composed intensity field is shown in Fig. 10, where the intensities for the red, green and blue beams (Fig. 9) have been added. As happened with the chessboard-like zone plates the intensity image of Fig. 10 is magnified with respect to that of Fig. 9, highlighting the effect of aberrations and misalignments in the image corresponding to experimental data, Fig. 9b).

The intensity distributions depicted in Fig. 9 show good agreement between experiment and simulation, with similar results than that of the chessboard-based design. Again, the achromaticity of the design is proved as the red and blue beams are focused while the green one is clearly out of focus. As with the chessboard-based design, there is a loss of symmetry in the experimental realizations that can be explained by the effect of aberrations.

The beam tomographies depicted in Fig. 11 also exhibit a good agreement between experiment and simulation. As expected, the red and blue beams are focused at the focal length of 380 mm, while the green beam focused ahead of this common focal point. For completeness, a composed intensity field is shown in Fig. 12, where the intensities for the red, green and blue beams (Fig. 11) have been added.

Finally, to gain further insight into the optical properties of the achromatic zone plates, we compared the beam intensity along the z-axis (axial intensity distribution) at the centre of the beam for both achromatic designs with a traditional Fresnel zone plate. Fig. 13a) shows the simulated (solid line) and experimental (circles) axial intensity distribution of a Fresnel zone plate with a focal distance of 380 mm for the design wavelength of 518 nm. Both the simulation and experiment demonstrate the standard chromatic behaviour of the Fresnel zone plate, with the red beam focussing ahead of the green and blue ones, as expected. The differences between the experimental and simulated profiles are due to aberrations and other experimental factors such as misalignments, noise, etc. However, there is still a good agreement between the simulation and the experiment.

Comparing this axial intensity distribution with those obtained for the chessboard-based zone plate (Fig. 13b) and random pixel-based zone plate (Fig. 13c) we can appreciate the achromatic behaviour of these zone plates, as well as the overall good agreement between experiment and simulation.

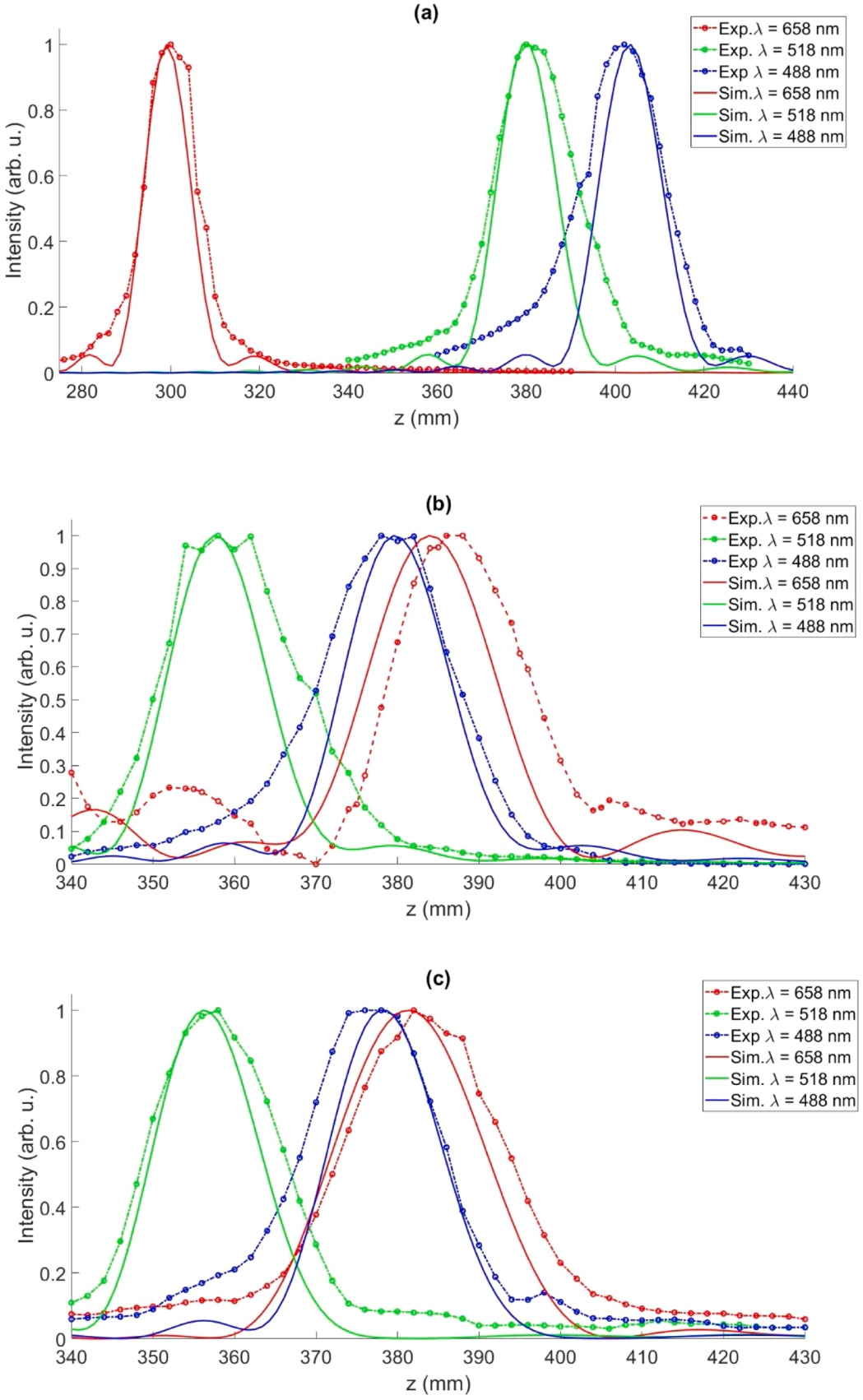

Fig. 13. Normalized intensities at beam centre along the Z-axis for a) a Fresnel zone plate of focal length 380 mm and a design wavelength of 518 nm, b) the Chessboard-based achromatic Fresnel Zone Plate shown in Fig. 3a), and c) the realization of the random pixel-based achromatic zone plate shown in Fig. 3b). The continuous lines correspond to simulations, while the circles correspond to the experimental results.

5. Conclusions

In this manuscript, a new kind of diffractive binary achromatic zone plate is proposed and both numerically and experimentally tested. It is defined as a chessboard inspired multiplexing of two zone plates designed for the Fraunhofer lines C and F, with a posterior special filtering and sub-Nyquist resolution. Thus, we achieve a zone plate with achromatic behavior and smooth edges between consecutive zones. We compare its behavior with other proposals based on the random pixel multiplexing of the same two zone plates. It results in a similar behavior, but our proposal presents a smoother appearance without the high-frequency irregularities of the random-based design that could be more resistant to manufacturing errors. The proposed zone plate could result of interest in visual optics, imaging, lithography, or solar concentration.

CRediT authorship contribution statement

Sara Fernandez-Nuñez: Writing – review & editing, Writing – original draft, Methodology, Formal analysis, Data curation, Conceptualization. **Jose Antonio Gomez-Pedrero:** Writing – review & editing, Writing – original draft, Software, Methodology, Conceptualization. **Francisco Jose Torcal-Milla:** Writing – review & editing, Writing – original draft, Software, Methodology, Conceptualization. **Luis Miguel Sanchez-Brea:** Writing – review & editing, Project administration, Funding acquisition.

Declaration of competing interest

The authors declare that they have no known competing financial interests or personal relationships that could have appeared to influence the work reported in this paper.

Acknowledgments

This work has been partially funded by project PID2021–122486OA-I00, financed by the Spanish Agencia Espacial de Investigación and the European Fund for Regional Development, and by "VDOEST" PID2022–138071OB-I00 grant, funded by MCIN / AEI / 10.13039/501100011033// FEDER, EU.

Data availability

Data will be made available on request.

References

[1] Born M, Wolf E. Principles Of Optics. 6th ed. Cambridge: Cambridge University Press; 2019.
[2] Leutz R, Ries H. Chromatic correction of Fresnel lens solar concentrators by means of diffractive optical elements in silicone. In: AIP Conference Proceedings. 2550. AIP Publishing; 2022. p. 1. September.
[3] Edmund Optics. Chromatic and monochromatic optical aberrations. Available at, https://www.edmundoptics.es/knowledge-center/application-notes/optics/chromatic-and-monochromatic-optical-aberrations/; 2025 [Accessed on February, 21st,.
[4] Hu H, Jiang T, Chen Y, Xu Z, Li Q, Feng H. Elimination of varying chromatic aberrations based on diffractive optics. Opt Express 2023;31:11041–52. https://doi.org/10.1364/OE.480628.
[5] Antonov AI, Greisukh GI, Ezhov EG, et al. Diffractive elements for imaging optical systems. Optoelectron Instrum Proc 2017;53:421–30. https://doi.org/10.3103/S8756699017050016.
[6] O'Shea DC, Suleski TJ, Kathman AD, Prather DW. Diffractive Optics: Design, Fabrication, And Test. 1st ed. Bellingham: SPIE Press; 2003.
[7] Wang P, Mohammad N, Menon R. Chromatic-aberration-corrected diffractive lenses for ultra-broadband focusing. Sci Rep 2016;6:21545. https://doi.org/10.1038/srep21545.
[8] Khonina SN, Kharitonov SI, Volotovsky SG. Evaluating the influence of the refractive index dispersion of a harmonic lens on focusing properties. In: Proc. SPIE 11516, Optical Technologies for Telecommunications; 2019, 115160B. https://doi.org/10.1117/12.2565126. 22 May 2020.
[9] Tan Y, Wu H, Wang S, Li C, Dai D. Silicon-based hybrid demultiplexer for wavelength- and mode-division multiplexing. Opt Lett 2018;43:1962–5. https://doi.org/10.1364/OL.43.001962.
[10] He Y, Zhang Y, Wang H, Sun L, Su Y. Design and experimental demonstration of a silicon multi-dimensional (de)multiplexer for wavelength-, mode- and polarization-division (de)multiplexing. Opt Lett 2020;45:2846–9. https://doi.org/10.1364/OL.390015.
[11] Gunawan W-H, Liu Y, Chow C-W, Chang Y-H, Yeh C-H. High speed visible light communication using digital power domain multiplexing of orthogonal frequency division multiplexed (OFDM). Signals Photonics 2021;8(11):500. https://doi.org/10.3390/photonics8110500.
[12] Millán MS, Otón J, Pérez-Cabré E. Dynamic compensation of chromatic aberration in a programmable diffractive lens. Opt Express 2006;14(20):9103–12. https://doi.org/10.1364/OE.14.009103.
[13] Pereiro-García J, Caño-García M, Blanco-Fernández O, Ramos-Uña R, Quintana X, Geday MA. Chromatic aberration compensation using thin, transparent, large aperture, wide focal range, adaptive liquid crystal lens. Opt Laser Technol 2025;180:111532. https://doi.org/10.1016/j.optlastec.2024.111532.
[14] Kazanskiy NL, Khonina SN, Karpeev SV, Porfirev AP. Diffractive optical elements for multiplexing structured laser beams. Quantum Elec (Woodbury) 2020;50(7):629–35. https://doi.org/10.1070/QEL17276.
[15] McManamon PF, Dorschner TA, Corkum DL, Friedman LJ, Hobbs DS, Holz M, Liberman S, Nguyen HQ, Resler DP, Sharp RC, Watson EA. Optical phased array technology. In: Proceedings of IEEE. 84; 1996. p. 268–98. https://doi.org/10.1109/5.482231.
[16] Xiao F, Kong L. Optical multi-beam forming method based on a liquid crystal optical phased array. Appl Opt 2017;56(36):9854–61. https://doi.org/10.1364/AO.56.009854.
[17] Rosen J, Alford S, Allan B, et al. Roadmap on computational methods in optical imaging and holography [invited]". Appl Phys 2024;B 130:166. https://doi.org/10.1007/s00340-024-08280-3.
[18] Shi R, Hu S, Sun C, Wang B, Cai Q. Broadband achromatic metalens in the visible light spectrum based on fresnel zone spatial multiplexing. Nanomaterials 2022;12(23):4298. https://doi.org/10.3390/nano12234298.
[19] Guo K, Wang C, Kang Q, Chen L, Guo Z. Broadband achromatic metalens with polarization insensitivity in the mid-infrared range. Opt Mater 2022;131:112489. https://doi.org/10.1016/j.optmat.2022.112489.
[20] Márquez A, Lemmi C, Campos J, Yzuel MJ. Achromatic diffractive lens written onto a liquid crystal display. Opt Lett 2006;31:392–4. https://doi.org/10.1364/OL.31.000392.
[21] Márquez A, Li C, Beléndez A, Maier SA, Ren H. Information multiplexing from optical holography to multi-channel metaholography. Nanophotonics 2023;12(24):4415–40. https://doi.org/10.1515/nanoph-2023-0605.
[22] Eisenbach O, Avayu Ditcovski R, Ellenbogen T. Metasurfaces based dual wavelength diffractive lenses. Opt Exp 2015;23(4):3928–36. https://doi.org/10.1364/OE.23.003928.
[23] Luo Z, Li Y, Semmen J, et al. Achromatic diffractive liquid-crystal optics for virtual reality displays. Light Sci Appl 2023;12:230. https://doi.org/10.1038/s41377-023-01254-8.
[24] Fernández R, Gallego S, Márquez A, Neipp C, Calzado EM, Francés J, Morales-Vidal M, Beléndez A. Complex diffractive optical elements stored in photopolymers. Polymers 2019;11:1920. https://doi.org/10.3390/polym11121920.
[25] Bravo JC, Sirvent-Verdú JJ, Colomina-Martínez J, Reyna Fernández R, Márquez A, Gallego S. Multifocal Fresnel lenses with adjustable focal points recorded in photopolymers. Opt Exp 2025;33(12):26499.
[26] Sonka M, Hlavac V, Boyle R. Image Processing, Analysis And Machine Vision. 3rd ed. Toronto: Thomson Learning; 2008.
[27] HOLOEYE Photonics AG.. PLUTO-2 phase only spatial light modulators. Device Oper Instr 2019.
[28] Hu Y, Wang Z, Wang X, et al. Efficient full-path optical calculation of scalar and vector diffraction using the Bluestein method. Light Sci Appl 2020;9:119. https://doi.org/10.1038/s41377-020-00362-z.
[29] Hu Y. Bluestein-method [software] GitHub. Available at, https://github.com/yanleihu/Bluestein-Method; 2024.